MATERIALS SCIENCE

Electronic structure orientation as a map of in-plane antiferroelectricity in β′-In_2Se_3

Joseph L. Spellberg[1,2], Lina Kodaimati[1], Prakriti P. Joshi[2], Nasim Mirzajani[1,2], Liangbo Liang[3], Sarah B. King[1,2]*

Antiferroelectric (AFE) materials are excellent candidates for sensors, capacitors, and data storage due to their electrical switchability and high-energy storage capacity. However, imaging the nanoscale landscape of AFE domains is notoriously inaccessible, which has hindered development and intentional tuning of AFE materials. Here, we demonstrate that polarization-dependent photoemission electron microscopy can resolve the arrangement and orientation of in-plane AFE domains on the nanoscale, despite the absence of a net lattice polarization. Through direct determination of electronic transition orientations and analysis of domain boundary constraints, we establish that antiferroelectricity in β′-In_2Se_3 is a robust property from the scale of tens of nanometers to tens of micrometers. Ultimately, the method for imaging AFE domain organization presented here opens the door to investigations of the influence of domain formation and orientation on charge transport and dynamics.

INTRODUCTION

Antiferroelectric (AFE) materials, featuring antiparallel, switchable, permanent dipoles (*1*, *2*), are excellent for energy-dense capacitors (*3*) and memory devices with robust storage capabilities (*4*, *5*). Rational design and development of AFE materials, however, have wrestled with the challenge of imaging AFE domains on the nanoscale to determine, for example, how nanoscale and mesoscale electronic properties arise from atomic structure (*6*). Given the lack of a net permanent dipole in AFE materials, piezoresponse force microscopy (PFM) offers little to no domain contrast, depending on a material's electrostriction coefficient. Furthermore, PFM cannot provide information on the orientation of domains, only that domains are different (*7*–*9*). Ferroic domains, such as those in AFE materials, are commonly on the order of tens to hundreds of nanometers (*10*, *11*), below the optical diffraction limit, making ferroic domains challenging to study with optical microscopy. Methods such as scanning tunneling microscopy (STM) and scanning transmission electron microscopy (STEM) that can resolve AFE domains by imaging atomic positions are challenging to scale from the nanoscale to the micrometer scale as point-scanning techniques. Both methods are also challenging to combine with ultrafast imaging methods, and STEM requires electron-transmissive samples. These challenges have not only inhibited material development but also made it extremely challenging to determine how AFE domain formation affects other critical properties, such as excited-state dynamics, known to be important in other ferroic materials (*12*). Here, we introduce how polarization-dependent photoemission electron microscopy (PD-PEEM) can image in-plane AFE domains, demonstrating a new way to resolve in-plane AFE domain structure on the nanoscale, and apply this technique to β′-In_2Se_3.

Indium(III) selenide (In_2Se_3) is a semiconductor with a complex phase diagram that includes two-dimensional van der Waals ferroelectric and AFE phases (*13*–*19*). The metastable β′ phase, which forms in thin-film samples due to substrate interactions when cooling from the high-temperature β phase (*13*–*19*), exhibits in-plane ferroelasticity and antiferroelectricity down to the monolayer limit (*1*, *7*, *20*). Antiferroelectricity occurs in β′-In_2Se_3 due to a nanostripe superstructure that forms as it cools from the hexagonal, high-temperature β phase (*13*, *15*). The nanostripes form along any one of three symmetrically equivalent $[11\bar{2}0]$ lattice vectors, defined by the structure of the symmetric high-temperature β phase, and have been observed with STM, STEM, and electron diffraction (*7*, *15*, *21*, *22*). Adjacent nanostripes are composed of antiparallel atomic displacements resulting in the lack of a net permanent dipole moment (Fig. 1A) (*20*, *23*).

Here, we show how PD-PEEM can image the AFE domains of β′-In_2Se_3 on the nanoscale by directly measuring the energy- and polarization-dependent transition dipole moment (TDM). Previous PEEM studies have successfully imaged ferroelectric and ferromagnetic domains, but these studies have relied on x-ray and ultraviolet excitation to induce single-photon photoemission (PE), rather than probing optical transitions as in this work, and to date, those methods have not been used to resolve AFE domains (*24*–*28*). Despite having zero net permanent dipole, the small atomic distortions that give rise to the AFE nature of β′-In_2Se_3 lead to electronic structure modifications that can be observed with PD-PEEM. Our method identifies AFE domain orientation, routinely achieves <100-nm spatial resolution—as good as 10-fold enhanced resolution compared to standard optical birefringence—and allows the identification of AFE properties inaccessible to conventional optical microscopy. Using first-principles density functional theory (DFT), we calculate the photon energy–dependent TDMs and match our calculations with experimentally measured photon energy–dependent maps of TDM orientations. We use this technique to demonstrate how the simultaneous nanoscale spatial resolution and wide-field imaging of PD-PEEM enable detailed analysis of AFE domain patterns, showing that the AFE domains of β′-In_2Se_3 are robust across tens of micrometers. This work opens a new way to probe antiferroelectricity on the nanoscale and sets the stage for further investigations of the unique electronic structure at ferroic domain boundaries such as charge transport (*12*, *29*), carrier lifetimes (*30*), and electrical properties (*31*).

[1]Department of Chemistry, University of Chicago, Chicago, IL 60637, USA. [2]James Franck Institute, University of Chicago, Chicago, IL 60637, USA. [3]Center for Nanophase Materials Science, Oak Ridge National Laboratory, Oak Ridge, TN 37831, USA. *Corresponding author. Email: sbking@uchicago.edu

RESULTS

Imaging domains with PD-PEEM

Contrast in PD-PEEM arises from the dependence of PE intensity on the angle between the laser electric field polarization (θ_E) and material's local TDM (θ_{TDM}), as shown schematically in Fig. 1 (B and C). This technique has been used previously to image the localized electronic states in black phosphorus (*32*) and polymer packing alignment (*33*). The PE intensity is maximized at the θ_E that is parallel to the θ_{TDM}, and the relationship between PE intensity and θ_E is defined by

$$I_{PE}(\theta) = A\cos^2(\theta_E - \theta_{TDM}) + C \quad (1)$$

where A is the amplitude of the modulation and C is the nonpolarization-dependent PE baseline. A detailed description of the optical selection rules of PD-PEEM can be found in (*32*). Incrementally rotating through the full 180° range of laser polarization, we observe the domains of β′-In_2Se_3 by their polarization-dependent PE intensity. Figure S3 shows examples of PD-PEEM images of a β′-In_2Se_3 flake. To better visualize the domains, we generate difference images by subtracting each image with laser excitation θ_E from the image acquired with the orthogonal laser polarization (θ_E + 90°). A movie showing PE intensity with respect to rotating θ_E is included in the Supplementary Materials. Figure 1D shows the difference image between PD-PEEM images recorded at θ_E = 140° and θ_E = 50° where bright regions correspond to θ_{TDM} = 140°. Integrating the PE intensity over the three indicated regions of interest and fitting to Eq. 1 (Fig. 1E), we identify three domain orientations offset from each other by ~60° ($\theta_{TDM,1}$ = 19 ± 3°, $\theta_{TDM,2}$ = 77 ± 2°, and $\theta_{TDM,3}$ = 140 ± 3°) comprising a threefold symmetric set of directions in the 180° range of unique θ_E.

By fitting the PE intensity of every pixel to the difference images as a function of θ_E, we can directly map the local θ_{TDM} alignment. To improve signal quality, we apply 2 × 2 pixel binning before fitting. A θ_{TDM} map of β′-In_2Se_3 with $h\nu$ = 3.1 eV (Fig. 1F) shows the characteristic cross-hatch domain pattern seen previously in optical birefringence experiments (*20*). Optical and atomic force microscopy (AFM) images of the same flake (fig. S4) show that the observed contrast does not originate from topographical features but is due to local variations in electronic structure and domain orientation. There are predominantly three domain orientations (resolved as blue, cyan, and brown) (*34*, *35*), each containing one of the regions of interest. This threefold symmetry is consistent with domains of similarly oriented nanostripes, which can exist along one of the three symmetric $[11\bar{2}0]$ lattice vectors.

PD-PEEM provides several notable advantages for imaging domains with different θ_{TDM} in comparison to other techniques, as summarized in table S1. First, PD-PEEM is a wide-field laser-based technique easily compatible with ultrafast spectroscopy (*36*–*38*), unlike STM and STEM. Second, there is a wider range of unique θ_E that results in observable contrast in PD-PEEM compared to optical birefringence, one of the standard methods for imaging of AFE domains. Figure 2A schematically shows possible arrangements of domains in a material with in-plane polarization, and Fig. 2 (B and C) shows how these domains would be observed by optical birefringence and PEEM, respectively. The periodicity of intensity with respect to laser polarization for optical birefringence is 90° (*39*, *40*).

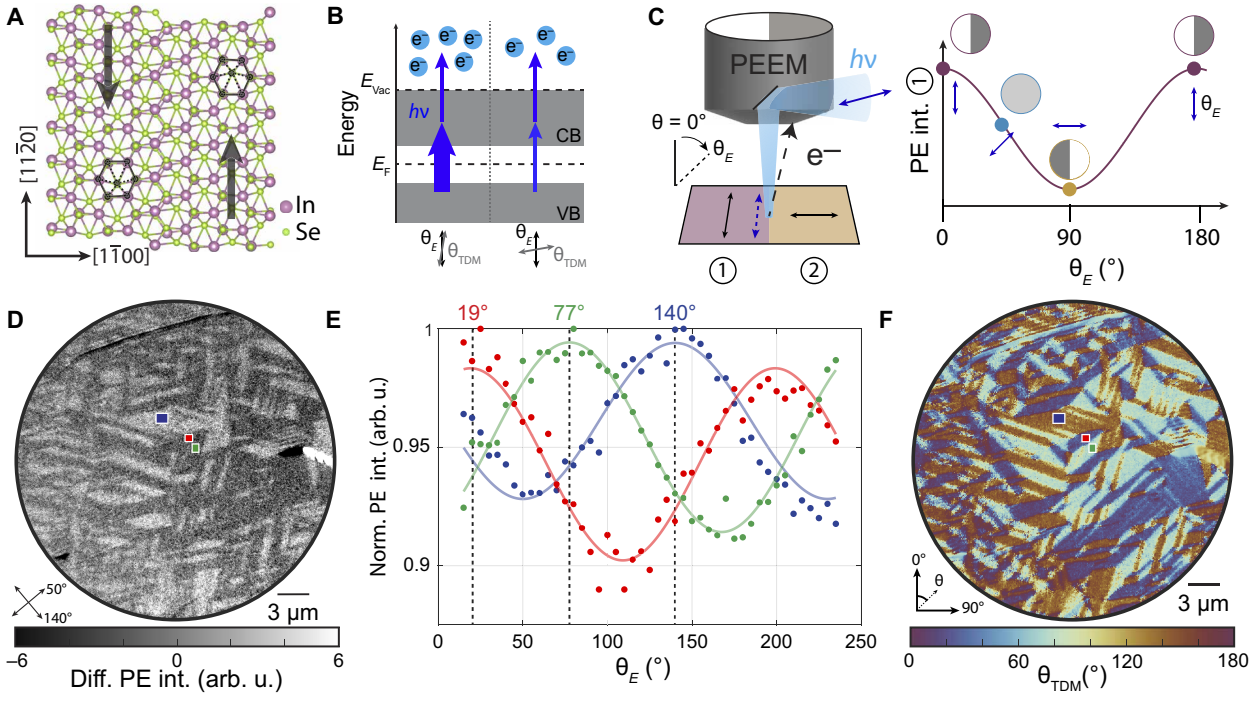

Fig. 1. Polarization-dependent imaging of β′-In_2Se_3. (**A**) Atomic structure of a supercell of β′-In_2Se_3. (**B**) Energy-level diagram of polarization-dependent two-photon PE process. CB, conduction band; VB, valence band. (**C**) Schematic of PD-PEEM for spatially dependent θ_{TDM}. White shading indicates maximum PE intensity. (**D**) Difference image from PD-PEEM with $h\nu$ = 3.1 eV. (**E**) PE intensity versus laser polarization from the three regions indicated. Dots are normalized PE intensity, and curves are fits to Eq. 1 regions in (D). (**F**) Map of θ_{TDM} fit to each 2 × 2 binned pixel in the difference PD-PEEM data. Maps of R^2 for all pixel-by-pixel fittings are shown in fig. S5. arb. u., arbitrary units.

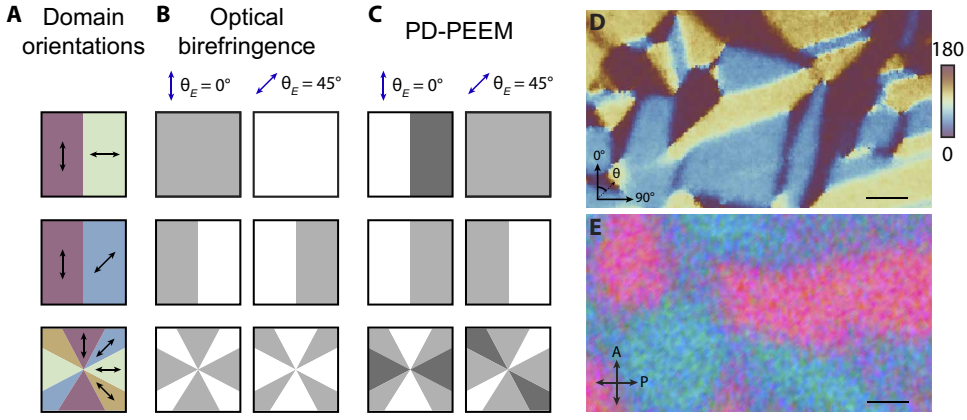

Fig. 2. Comparison of optical birefringence and PD-PEEM. (**A**) Schematic of different domain structures where the arrows indicate spatially variant θ_{TDM}. (**B**) Schematic of visualization of the same domains using optical birefringence. (**C**) Schematic of visualization of different domain orientations in PD-PEEM. In both schematics, white indicates greater intensity measured at the detector and gray indicates less intensity. (**D**) θ_{TDM} map from PD-PEEM on a β′-In_2Se_3 flake with $h\nu = 3.1$ eV. Scale bar, 1 μm. (**E**) Optical birefringence image of β′-In_2Se_3 with the same scale as in (D), where "P" and "A" are the directions of the optical polarizer and analyzer, respectively.

This means that θ_{TDM} directions (which often correspond to the birefringent axis) cannot be determined uniquely with this method because two perpendicular orientations would equally rotate the incident light and produce the same image (Fig. 2B). Similarly, domains oriented perpendicular to each other cannot be separately resolved, regardless of the incident polarization (*40*). PEEM intensity, however, has 180° periodicity with respect to laser polarization, meaning that all domain orientations can be uniquely identified. Therefore, PD-PEEM provides information regarding the alignment of domains that optical birefringence cannot resolve (Fig. 1C). Third, electron imaging is bounded by a lower diffraction limit compared to imaging with photons. PEEM imaging allows the identification of features smaller than the optical diffraction limit (*32*) while retaining wide-field spectroscopic capabilities, which enables faster imaging and domain analysis over larger regions compared to point-scanning techniques. A map of β′-In_2Se_3 domains from a zoomed-in field of view (Fig. 2D) shows readily apparent small features on the order of 100 nm that would be lost when imaging with a lower-resolution technique such as optical microscopy (Fig. 2E). The flake in Fig. 2E is on a thick layer of SiO_2 to boost contrast, while the PEEM experiments are conducted on Si substrates with native oxide. An example of both methods applied to the same flake is shown in fig. S6. Comparisons of the spatial resolution of these two methods are shown in figs. S7 to S9, where we can achieve a spatial resolution as good as 51 nm with PD-PEEM, a 10-fold improvement over optical birefringence.

Energy-dependent TDM

To better understand the contrast mechanism enabling the observation of β′-In_2Se_3 domains with PD-PEEM, we performed DFT calculations to determine the frequency-dependent dielectric function and optical transition matrix of a supercell of β′-In_2Se_3. Using previously published atomic positions for a supercell of the AFE lattice measured experimentally (*20*), we calculated the band structure and TDM angle with respect to nanostripe direction for a range of excitation energies from 1.3 to 3.4 eV, corresponding to across bandgap transitions in the PEEM measurements. Although β′-In_2Se_3 has no net permanent dipole, DFT confirms that there is polarization anisotropy in across bandgap transitions. The magnitude of this anisotropy is quantified by the linear optical dichroism as discussed in the Supplementary Materials. The calculated optical dichroism, the gray trace in Fig. 3, varies for different excitation energies but is nonzero across the calculated range with a mean of ~0.3. The atomic distortions, which give rise to the nanostripe superstructure in β′-In_2Se_3, create electronic structure anisotropy that can be probed with polarization-dependent photoexcitation. In addition to confirming the nonzero dichroism, our calculations also predict that the TDM is oriented either parallel or perpendicular to the nanostripe direction, depending on the excitation energy. The black points in Fig. 3 show that these are the only directions that the TDM orientation can take. There is no particular energy where the TDM angle changes, but rather the orientation varies as a function of photon energy. Polar plots showing absorption intensity versus polarization angle for two excitation energies are shown in the inset. Absorption of $h\nu$ = 2.40 eV (orange curve) is oriented along the nanostripe direction and has relatively strong dichroism; absorption of $h\nu$ = 3.05 eV (blue curve) is perpendicular to the nanostripe direction and has much weaker, but still nonzero, dichroism.

This binary selection of allowed values for θ_{TDM} is consistent with the 180° periodicity observed in the PD-PEEM response. The laser aligns with the θ_{TDM} only once for each 180° rotation and suggests that θ_{TDM} is restricted to be oriented parallel or perpendicular to the stripe direction (fig. S10), which is consistent with optical dichroism and birefringence experiments (*7*, *15*, *20*).

We confirmed the energy dependence of the TDM orientation and dichroism experimentally. Figure 4 (A and B) shows maps from two polarization-dependent PEEM experiments on a β′-In_2Se_3 flake that was illuminated with 3.06 and 2.40 eV photons, respectively. These excitation energies result in two- and three-photon processes (fig. S11). While the same domain patterns are observed in both images, θ_{TDM} measured in each domain is phase shifted by ~90° ($\theta_{TDM,306\ eV} = 110 \pm 5°$ and $\theta_{TDM,2.40eV} = 194 \pm 6°$) between the two measurements (Fig. 4C and fig. S12), in agreement with the DFT prediction. The PE response for both excitation energies has low dichroism, but it is stronger for $h\nu = 2.40$ eV, consistent with the variability in dichroism predicted by DFT. While limitations on DFT's

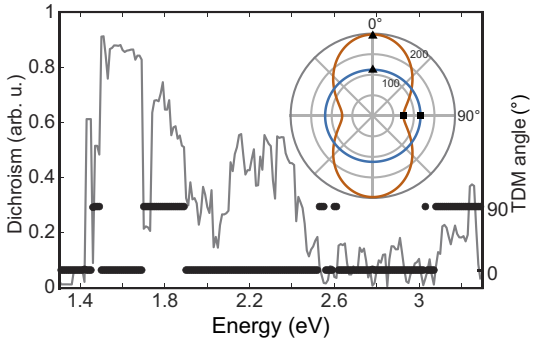

Fig. 3. Optical dichroism and TDM angle versus $h\nu$ for across bandgap transitions in β′-In_2Se_3. (**Inset**) Polar plot of transition intensity for $h\nu = 2.40$ eV (orange) and $h\nu = 3.05$ eV (blue). Distance from origin is the strength of photoabsorption, and angle is the polarization orientation. Triangles indicate parallel to nanostripes, and squares are perpendicular.

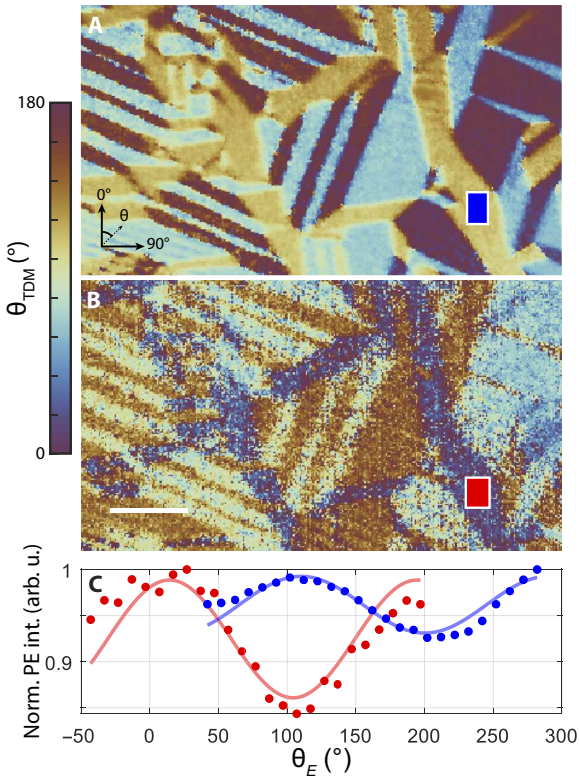

Fig. 4. Wavelength dependence of PD-PEEM. Maps of θ_{TDM} for β′-In_2Se_3 illuminated with (**A**) $h\nu = 3.06$ eV and (**B**) $h\nu = 2.40$ eV, scale bar 3 μm. (**C**) Traces of PE intensity versus θ_E for the indicated regions in (A) and (B).

energetic accuracy prevents our energy-dependent results from being used to assign lattice directions, the agreement between experiment and theoretical calculations suggests that the across bandgap TDMs in β′-In_2Se_3 are preferentially oriented parallel or perpendicular to the nanostripe direction, depending on $h\nu$ and which electronic states are coupled with a photon.

Domain boundary orientations

To demonstrate how nanoscale domain resolution combined with a wide field of view enables detailed analysis of AFE materials, we analyzed the geometry of domains and domain boundary arrangements observed in the PD-PEEM data. Previous atomic-scale STEM imaging of individual domain walls in β′-In_2Se_3 established that the formation of boundaries between AFE domains is governed by three geometric rules, which we analyze and confirm in our experiments by measuring boundary orientations across the entire field of view (Fig. 5A and figs. S13 and S14), namely, (i) nanostripes form along the $[11\bar{2}0]$ lattice directions, (ii) domain walls can form in six discrete directions along either the $[11\bar{2}0]$ or $[1\bar{1}00]$ lattice vectors, and (iii) domain boundaries always bisect the angle formed by adjacent nanostripes (*7*, *20*). These three rules, as illustrated schematically in Fig. 5B, establish both which domain shapes are possible and how nanostripes can and cannot orient within domains. A complete geometric analysis describing how these rules extend to larger spatial scales and how domains and domain boundaries can be combined to make different geometric patterns is included in the Supplementary Materials (figs. S15 to S18). Here, we show that the domain patterns observed in PD-PEEM are fully consistent with the geometry defined by atomic-scale nanostripes, directly connecting the domains resolved over a 30-μm field of view to the atomic distortions in the lattice that give rise to antiferroelectricity.

We measured the angles of the domain wall boundaries of the flake discussed in Fig. 1 across the entire 30-μm field of view (fig. S13) and constructed a histogram of the angle of each domain boundary with respect to the coordinate system of the PEEM image (Fig. 5C). The angles of the domain walls are grouped into six discrete orientations, spaced by 30 ± 5°. Each specific domain wall direction corresponds to a unique pair of domain orientations. For example, all domain walls with an angle of about 20° (cluster A; indicated in yellow) correspond to boundaries between domains with $\theta_{TDM} \backsimeq 80°$ and 140° (resolved as cyan and brown, respectively, in Figs. 1F and 5A). Similarly, every other boundary orientation uniquely corresponds to a pair of domains (Fig. 5D). The histogram clusters can be divided into perpendicular pairs. For example, boundary classes A and D separate the same two domain types ($\theta_{TDM} \backsimeq 80°$ and 140°) and are oriented about 90° from each other. The same correspondence between perpendicular domain boundaries is true for the other four directions.

These findings are all consistent with two perpendicular, threefold symmetric sets of boundary orientations ($[11\bar{2}0]$ or $[1\bar{1}00]$). We also identify the rotation of θ_{TDM} between adjacent domains $\Delta\theta_{TDM}$ to be 60° or 120° and the angle is bisected by their boundary, as illustrated in Fig. 5D. These are the same angles that nanostripes form at boundaries, as determined by STEM (*7*), confirming that the atomic nanostripe directions and θ_{TDM} values have equivalent relationships to the boundaries that contain them. Therefore, these two quantities must be aligned along the same two axes. The shape and orientation of a particular domain restrict the nanostripe direction and θ_{TDM} that it can contain (discussed in detail in the Supplementary Materials). From this, we can confirm that the two optical axes identified with the energy-dependent measurement are oriented parallel and perpendicular to the nanostripe direction, further supporting the DFT calculations (fig. S19).

Each of the three "rules" for β′-In_2Se_3 AFE domains are rigorously consistent for the micrometer domains observed with PD-PEEM

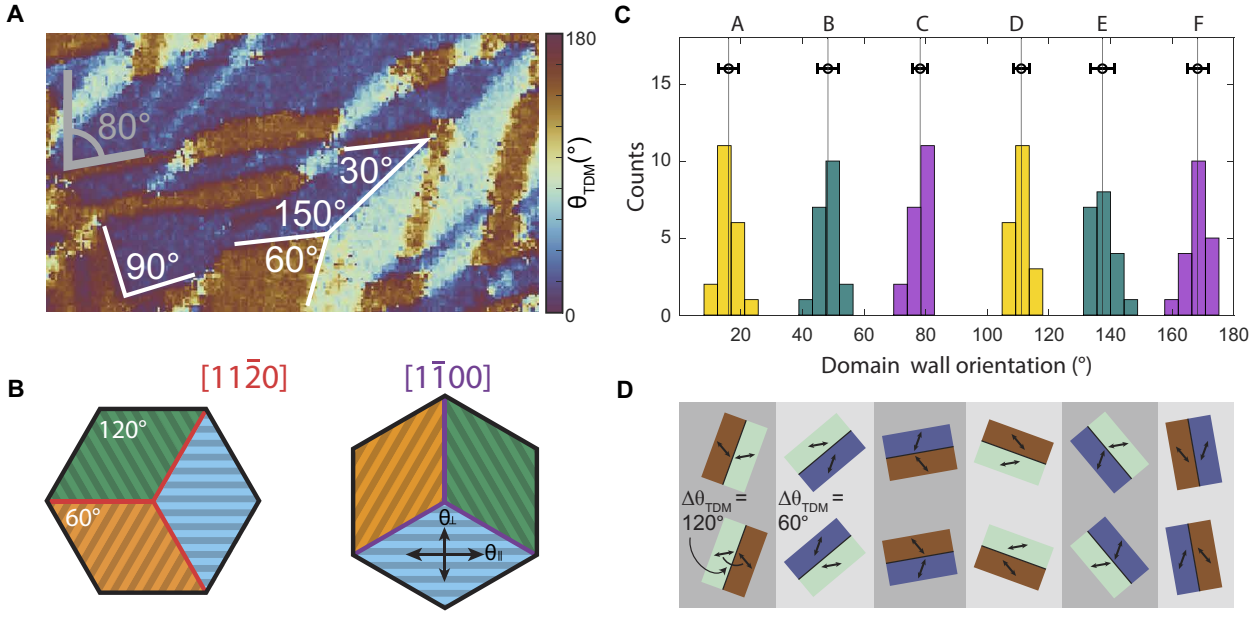

Fig. 5. Domain boundary orientations. (**A**) Region from the θ_{TDM} map in Fig. 1F. Domain boundary angles are measured with respect to the image vertical axis; white lines indicate domain interior angles. (**B**) Schematic of domain walls along the [11$\bar{2}$0] and [1$\bar{1}$00] directions. Orange, blue, and green regions indicate domains with different nanostripe orientations. (**C**) Histogram of domain wall orientations from PD-PEEM data shown in Fig. 1F. Black circles indicate the mean domain wall orientation and error of each cluster. (**D**) Domains separated by each boundary orientation in (A) according to θ_{TDM} directions measured with PD-PEEM. Double-headed arrows indicate TDM direction and always form an angle that is bisected by the domain boundary.

across the entire 30-μm field of view and across multiple flakes (fig. S14). While we cannot specify which optical axis corresponds to which lattice vector, the energy-dependent measurement in conjunction with the shape analysis confirms that the electronic structure orientation is dictated by the atomic distortions such that θ_{TDM} is always parallel or perpendicular to the nanostripe direction. This analysis is only possible because of the simultaneous spatial resolution and field of view of PD-PEEM and shows the opportunities that this technique provides in understanding the nanoscale and mesoscale structure of AFE materials (*37*).

DISCUSSION

In this work, we use PD-PEEM to image the in-plane AFE domain structure of β′-In_2Se_3 over multiple length scales from tens of nanometers to tens of micrometers with <100-nm spatial resolution. We use these capabilities to show that the domain structure of β′-In_2Se_3 is highly robust and shows an impressive degree of fidelity across large spatial regions and multiple samples.

The photon energy–dependent electronic transition orientation of β′-In_2Se_3 creates both challenges and opportunities in the future study of β′-In_2Se_3. Because the birefringence of a material is related to the optical TDM (*39*), we note that care must be taken when using optical measurements to study polarization or lattice directions in β′-In_2Se_3 given the variation in θ_{TDM} as a function of photon energy. When broadband white light is used, the measured angle of maximum photoabsorption will not necessarily align with the direction of AFE polarization; rather, the measured angle will represent a convolution of the simultaneous responses of multiple photon energies. This is further complicated by the nonuniform relationship between optical dichroism and excitation energy. However, in experiments with precise excitation energy, β′-In_2Se_3 presents an exciting platform for the investigation of anisotropic electronic structure and properties. The findings presented in this work show that PD-PEEM can accurately resolve domains even when there is no net lattice polarization. Even minor distortions, like those that form the nanostripes of β′-In_2Se_3, lead to electronic structure changes that are sufficiently strong to be readily resolved in PD-PEEM. Our results exemplify the opportunities for using PD-PEEM in studying the physics of in-plane ferroelectrics, antiferroelectrics, and other domain structures of materials.

MATERIALS AND METHODS

Sample preparation

In_2Se_3 flakes were mechanically exfoliated from a bulk crystal grown by chemical vapor transport (2D Semiconductors) under N_2 atmosphere. The flakes were transferred via polydimethylsiloxane stamp (*41*) onto Si with native oxide substrates and annealed on a hot plate at 300° to 350°C for 30 min. Upon cooling to room temperature, the β′ phase is produced (figs. S1 and S2). Samples were then observed in cross-polarized optical microscopy to verify the presence of AFE domains on the flakes. Subsequent characterization with AFM (Bruker MM8, ScanAsyst) and Raman microscopy (HORIBA LabRAM HR Evolution confocal Raman microscope) determined flakes thicknesses and phases, respectively. All flakes discussed in this work have thicknesses of a few hundreds of nanometers.

Photoemission electron microscopy

PE experiments were conducted in a PE electron microscope (Focus GmbH, Scienta Omicron GmbH). Laser illumination is directed to the chamber through a thin-film polarizer and a λ/2 waveplate on a

rotational stage. In the chamber, the laser beam reflects off a Rh mirror to be incident on the sample at 4° from the surface normal, causing the polarization to be effectively in the plane of the sample. Illumination is from an optical parametric chirped pulse amplifier (Class 5 Photonics; Figs. 1 and 5; figs. S3, S11, S14, A and B, and S18F; and movie S1), a home-built nonlinear optical parametric amplifier (Figs. 2D and 4A, and figs. S6C, S8, S9, S11A, S12A, and S19A), or the second harmonic of a 1035-nm laser (Coherent Monaco; Fig. 4B and figs. S11B, S12B, and S19B). All experiments were conducted with 4-MHz repetition rates.

Density functional theory

DFT calculations were performed using the Vienna ab initio simulation package (VASP; version 5.4.4), where the projector augmented wave method was used for pseudopotentials (*42*, *43*), and the electron exchange-correlation functional was chosen as the generalized gradient approximation of Perdew, Burke and Ernzerhof (*44*). The monolayer AFE nanostripe structure (*20*) was fully relaxed by the conjugate gradient scheme until the maximum force was less than 0.01 eV/Å on each atom. The total energy was converged to 10^{-6} eV. The energy cutoff of the plane waves was chosen as 350 eV. The k-point sampling in the Brillouin zone (BZ) corresponds to Γ-centered $1 \times 12 \times 1$ k-grid. In addition, a vacuum region of ~18 Å in the z direction was used to avoid spurious interactions between the neighboring cells. The optimized in-plane lattice constants are $a = 27.668$ Å and $b = 4.076$ Å while c is fixed to 25 Å. On the basis of the nanostripe structure, a $1 \times 7 \times 1$ supercell was built, for which only the Γ-point in the BZ was considered while other parameters are unchanged. For such a supercell, we computed its frequency-dependent dielectric function using VASP, which also generates the optical transition matrix elements between any valence and conduction states. These optical transition matrix elements enable us to obtain the TDM of a specific electronic excitation.

Supplementary Materials

This PDF file includes:

Supplementary Text
Figs. S1 to S19
Table S1
Legend for movie S1
References

Other Supplementary Material for this manuscript includes the following:

Movie S1

REFERENCES AND NOTES

1. Z. Liu, T. Lu, J. Ye, G. Wang, X. Dong, R. Withers, Y. Liu, Antiferroelectrics for energy storage applications: A review. *Adv. Mater. Technol.* **3**, 111 (2018).
2. C. A. Randall, Z. Fan, I. Reaney, L. Chen, S. Trolier-McKinstry, Antiferroelectrics: History, fundamentals, crystal chemistry, crystal structures, size effects, and applications. *J. Am. Ceram. Soc.* **104**, 3775–3810 (2021).
3. C. W. Ahn, G. Amarsanaa, S. S. Won, S. A. Chae, D. S. Lee, I. W. Kim, Antiferroelectric thin-film capacitors with high energy-storage densities, low energy losses, and fast discharge times. *ACS Appl. Mater. Interfaces* **7**, 26381–26386 (2015).
4. M. M. Vopson, X. Tan, Four-state anti-ferroelectric random access memory. *IEEE Electron Device Lett.* **37**, 1551–1554 (2016).
5. L. Liu, Y. Cai, X. Chen, Z. Liu, G. Yuan, Y. Wang, Flexible multi-state nonvolatile antiferroelectric memory. *J. Am. Ceram. Soc.* **105**, 6232–6240 (2022).
6. A. K. Tagantsev, K. Vaideeswaran, S. B. Vakhrushev, A. V. Filimonov, R. G. Burkovsky, A. Shaganov, D. Andronikova, A. I. Rudskoy, A. Q. R. Baron, H. Uchiyama, D. Chernyshov, A. Bosak, Z. Ujma, K. Roleder, A. Majchrowski, J.-H. Ko, N. Setter, The origin of antiferroelectricity in $PbZrO_3$. *Nat. Commun.* **4**, 2229 (2013).
7. C. Xu, J. Mao, X. Guo, S. Yan, Y. Chen, T. W. Lo, C. Chen, D. Lei, X. Luo, J. Hao, C. Zheng, Y. Zhu, Two-dimensional ferroelasticity in van der Waals β′-In_2Se_3. *Nat. Commun.* **12**, 3665 (2021).
8. Q. N. Chen, Y. Ou, F. Ma, J. Li, Mechanisms of electromechanical coupling in strain based scanning probe microscopy. *Appl. Phys. Lett.* **104**, 242907 (2014).
9. Y. Kim, A. Kumar, A. Tselev, I. I. Kravchenko, H. Han, I. Vrejoiu, W. Lee, D. Hesse, M. Alexe, S. V. Kalinin, S. Jesse, Nonlinear phenomena in multiferroic nanocapacitors: Joule heating and electromechanical effects. *ACS Nano* **5**, 9104–9112 (2011).
10. A. K. Tagantsev, L. E. C. Cross, J. Fousek, *Domains in Ferroic Crystals and Thin Films* (Springer, 2010).
11. J. E. F. Gonzales, A. Ganzha, M. Kniazeva, D. Andronikova, A. Vakulenko, A. Filimonov, A. Rudskoy, C. Richter, A. Dasgupta, R. Gao, R. Burkovsky, Thickness independence of antiferroelectric domain characteristic sizes in epitaxial $PbZrO_3/SrRuO_3/SrTiO_3$ films. *J. Appl. Cryst.* **56**, 697–706 (2023).
12. B. Guzelturk, A. B. Mei, L. Zhang, L. Z. Tan, P. Donahue, A. G. Singh, D. G. Schlom, L. W. Martin, A. M. Lindenberg, Light-induced currents at domain walls in multiferroic $BiFeO_3$. *Nano Lett.* **20**, 145–151 (2020).
13. J. van Landuyt, G. van Tendeloo, S. Amelinckx, Phase transitions in In_2Se_3 as studied by electron microscopy and electron diffraction. *Phys. Status Solidi A* **30**, 299–314 (1975).
14. C. Manolikas, New results on the phase transformations of In_2Se_3. *J. Solid State Chem.* **74**, 319–328 (1988).
15. C. Zheng, L. Yu, L. Zhu, J. L. Collins, D. Kim, Y. Lou, C. Xu, M. Li, Z. Wei, Y. Zhang, M. T. Edmonds, S. Li, J. Seidel, Y. Zhu, J. Z. Liu, W.-X. Tang, M. S. Fuhrer, Room temperature in-plane ferroelectricity in van der Waals In_2Se_3. *Sci. Adv.* **4**, eaar7720 (2018).
16. X. Tao, Y. Gu, Crystalline-crystalline phase transformation in two-dimensional In_2Se_3 thin layers. *Nano Lett.* **13**, 3501–3505 (2013).
17. X. Zheng, W. Han, K. Yang, L. W. Wong, C. S. Tsang, K. H. Lai, F. Zheng, T. Yang, S. P. Lau, T. H. Ly, M. Yang, J. Zhao, Phase and polarization modulation in two-dimensional In_2Se_3 via in situ transmission electron microscopy. *Sci. Adv.* **8**, eabo0773 (2022).
18. W. Han, X. Zheng, K. Yang, C. S. Tsang, F. Zheng, L. W. Wong, K. H. Lai, T. Yang, Q. Wei, M. Li, W. F. Io, F. Guo, Y. Cai, N. Wang, J. Hao, S. P. Lau, C.-S. Lee, T. H. Ly, M. Yang, J. Zhao, Phase-controllable large-area two-dimensional In_2Se_3 and ferroelectric heterophase junction. *Nat. Nanotechnol.* **18**, 55–63 (2023).
19. S. Wan, Q. Peng, Z. Wu, Y. Zhou, Nonvolatile ferroelectric memory with lateral β/α/β In_2Se_3 heterojunctions. *ACS Appl. Mater. Interfaces* **14**, 25693–25700 (2022).
20. C. Xu, Y. Chen, X. Cai, A. Meingast, X. Guo, F. Wang, Z. Lin, T. W. Lo, C. Maunders, S. Lazar, N. Wang, D. Lei, Y. Chai, T. Zhai, X. Luo, Y. Zhu, Two-dimensional antiferroelectricity in nanostripe-ordered In_2Se_3. *Phys. Rev. Lett.* **125**, 047601 (2020).
21. J. L. Collins, C. Wang, A. Tadich, Y. Yin, C. Zheng, J. Hellerstedt, A. Grubišić-Čabo, S. Tang, S.-K. Mo, J. Riley, E. Huwald, N. V. Medhekar, M. S. Fuhrer, M. T. Edmonds, Electronic band structure of in-plane ferroelectric van der Waals β′-In_2Se_3. *ACS Appl. Electron. Mater.* **2**, 213–219 (2020).
22. F. Zhang, Z. Wang, J. Dong, A. Nie, J. Xiang, W. Zhu, Z. Liu, C. Tao, Atomic-scale observation of reversible thermally driven phase transformation in 2D In_2Se_3. *ACS Nano* **13**, 8004–8011 (2019).
23. Z. Zhang, J. Nie, Z. Zhang, Y. Yuan, Y. Fu, W. Zhang, Atomic visualization and switching of ferroelectric order in β-In_2Se_3 films at the single layer limit. *Adv. Mater.* **34**, e2106951 (2022).
24. J. Schaab, I. P. Krug, F. Nickel, D. M. Gottlob, H. Döganay, A. Cano, M. Hentschel, Z. Yan, E. Bourret, C. M. Schneider, R. Ramesh, D. Meier, Imaging and characterization of conducting ferroelectric domain walls by photoemission electron microscopy. *Appl. Phys. Lett.* **104**, 232904 (2014).
25. N. Barrett, J. E. Rault, J. L. Wang, C. Mathieu, A. Locatelli, T. O. Mentes, M. A. Niño, S. Fusil, M. Bibes, A. Barthélémy, D. Sando, W. Ren, S. Prosandeev, L. Bellaiche, B. Vilquin, A. Petraru, I. P. Krug, C. M. Schneider, Full field electron spectromicroscopy applied to ferroelectric materials. *J. Appl. Phys.* **113**, 187217 (2013).
26. J. E. Rault, W. Ren, S. Prosandeev, S. Lisenkov, D. Sando, S. Fusil, M. Bibes, A. Barthélémy, L. Bellaiche, N. Barrett, Thickness-dependent polarization of strained $BiFeO_3$ films with constant tetragonality. *Phys. Rev. Lett.* **109**, 267601 (2012).
27. M. Ghidini, F. Maccherozzi, S. S. Dhesi, N. D. Mathur, XPEEM and MFM imaging of ferroic materials. *Adv. Electron. Mater.* **8**, 162 (2022).
28. A. Sander, M. Christl, C.-T. Chiang, M. Alexe, W. Widdra, Domain imaging on multiferroic $BiFeO_3$(001) by linear and circular dichroism in threshold photoemission. *J. Appl. Phys.* **118**, 224102 (2015).
29. J. M. Frost, K. T. Butler, F. Brivio, C. H. Hendon, M. van Schilfgaarde, A. Walsh, Atomistic origins of high-performance in hybrid halide perovskite solar cells. *Nano Lett.* **14**, 2584–2590 (2014).
30. X. Xiao, W. Li, Y. Fang, Y. Liu, Y. Shao, S. Yang, J. Zhao, X. Dai, R. Zia, J. Huang, Benign ferroelastic twin boundaries in halide perovskites for charge carrier transport and recombination. *Nat. Commun.* **11**, 2215 (2020).

31. X.-K. Wei, T. Sluka, B. Fraygola, L. Feigl, H. Du, L. Jin, C.-L. Jia, N. Setter, Controlled charging of ferroelastic domain walls in oxide ferroelectrics. *ACS Appl. Mater. Interfaces* **9**, 6539–6546 (2017).
32. P. P. Joshi, R. Li, J. L. Spellberg, L. Liang, S. B. King, Nanoimaging of the edge-dependent optical polarization anisotropy of black phosphorus. *Nano Lett.* **22**, 3180–3186 (2022).
33. A. Neff, F. Niefind, B. Abel, S. C. B. Mannsfeld, K. R. Siefermann, Imaging nanoscale morphology of semiconducting polymer films with photoemission electron microscopy. *Adv. Mater.* **29**, 1701012 (2017).
34. F. Crameri, G. E. Shephard, P. J. Heron, The misuse of colour in science communication. *Nat. Commun.* **11**, 5444 (2020).
35. F. Crameri, Scientific colour maps, version 8.0.1, Zenodo (2023) https://doi.org/10.5281/zenodo.8409685.
36. M. Aeschlimann, M. Bauer, D. Bayer, T. Brixner, F. J. G. de Abajo, W. Pfeiffer, M. Rohmer, C. Spindler, F. Steeb, Adaptive subwavelength control of nano-optical fields. *Nature* **446**, 301–304 (2007).
37. M. Dabrowski, Y. Dai, H. Petek, Ultrafast microscopy: Imaging light with photoelectrons on the nano-femto scale. *J. Phys. Chem. Lett.* **8**, 4446–4455 (2017).
38. M. K. L. Man, A. Margiolakis, S. Deckoff-Jones, T. Harada, E. L. Wong, M. B. M. Krishna, J. Madéo, A. Winchester, S. Lei, R. Vajtai, P. M. Ajayan, K. M. Dani, Imaging the motion of electrons across semiconductor heterojunctions. *Nat. Nanotechnol.* **12**, 36–40 (2017).
39. M. Sabooni, A. N. Nilsson, G. Kristensson, L. Rippe, Wave propagation in birefringent materials with off-axis absorption or gain. *Phys. Rev. A* **93**, 013842 (2016).
40. S. Haussühl, Physical Properties of Crystals (Wiley-VCH, 2007).
41. A. Castellanos-Gomez, M. Buscema, R. Molenaar, V. Singh, L. Janssen, H. S. J. van der Zant, G. A. Steele, Deterministic transfer of two-dimensional materials by all-dry viscoelastic stamping. *2D Mater.* **1**, 011002 (2014).
42. G. Kresse, J. Furthmüller, Efficient iterative schemes for ab initio total-energy calculations using a plane-wave basis set. *Phys. Rev. B* **54**, 11169–11186 (1996).
43. G. Kresse, D. Joubert, From ultrasoft pseudopotentials to the projector augmented-wave method. *Phys. Rev. B* **59**, 1758–1775 (1999).
44. J. P. Perdew, K. Burke, M. Ernzerhof, Generalized gradient approximation made simple. *Phys. Rev. Lett.* **77**, 3865–3868 (1996).
45. J. H. Weaver, C. G. Olson, D. W. Lynch, Optical investigation of the electronic structure of bulk Rh and Ir. *Phys. Rev. B* **15**, 4115–4118 (1977).
46. X. Ling, S. Huang, E. H. Hasdeo, L. Liang, W. M. Parkin, Y. Tatsumi, A. R. T. Nugraha, A. A. Puretzky, P. M. Das, B. G. Sumpter, D. B. Geohegan, J. Kong, R. Saito, M. Drndic, V. Meunier, M. S. Dresselhaus, Anisotropic electron-photon and electron-phonon interactions in black phosphorus. *Nano Lett.* **16**, 2260–2267 (2016).
47. F. Lyu, X. Li, J. Tian, Z. Li, B. Liu, Q. Chen, Temperature-driven α-β phase transformation and enhanced electronic property of 2H α-In_2Se_3. *ACS Appl. Mater. Interfaces* **14**, 23637–23644 (2022).
48. A. Rodger, B. Nordén, Circular Dichroism and Linear Dichroism (Oxford Univ. Press, 1997).
49. N. Shibata, Y. Kohno, A. Nakamura, S. Morishita, T. Seki, A. Kumamoto, H. Sawada, T. Matsumoto, S. D. Findlay, Y. Ikuhara, Atomic resolution electron microscopy in a magnetic field free environment. *Nat. Commun.* **10**, 2308 (2019).
50. L. Jones, S. Wang, X. Hu, S. U. Rahman, M. R. Castell, Maximising the resolving power of the scanning tunneling microscope. *Adv. Struct. Chem. Imaging* **4**, 7 (2018).
51. T. Esat, X. Yang, F. Mustafayev, H. Soltner, F. S. Tautz, R. Temirov, Determining the temperature of a millikelvin scanning tunnelling microscope junction. *Commun. Phys.* **6**, 81 (2023).
52. K. Liang, L. Bi, Q. Zhu, H. Zhou, S. Li, Ultrafast dynamics revealed with time-resolved scanning tunneling microscopy: A review. *ACS Appl. Opt. Mater.* **1**, 924–938 (2023).
53. A. Gruverman, M. Alexe, D. Meier, Piezoresponse force microscopy and nanoferroic phenomena. *Nat. Commun.* **10**, 1661 (2019).

Acknowledgments: We thank C. Ophus from the Lawrence Berkeley National Laboratory for helpful discussions regarding data analysis and K. Waters from the University of Chicago for assistance with manuscript preparation. **Funding:** This work was supported by the Office of Basic Energy Sciences, U.S. Department of Energy (DOE) [grant DE-SC0021950 (S.B.K.)]; University of Chicago Materials Research Science and Engineering Center, U.S. National Science Foundation [grant DMR-2011854 (shared facilities)]; University of Chicago Materials Research Science and Engineering Center, U.S. National Science Foundation [grant DMR-1420709 (shared facilities)]; University of Chicago Research Computing Center; Center for Nanophase Material Sciences, U.S. Department of Energy Office of Science User Facility (L.L.); University of Chicago MRSEC Kadanoff-Rice Fellowship [grants DMR-2011854 and DMR-1420709 (P.P.J.)]; and National Energy Research Scientific Computing Center, DOE Office of Science User Facility, Office of Science of the U.S. Department of Energy [under contract no. DE-AC02-05CH11231 (L.L.)]. **Author contributions:** Conceptualization: J.L.S., P.P.J., and S.B.K. Methodology: J.L.S., P.P.J., L.L., and S.B.K. Software: J.L.S., N.M., P.P.J., and L.L. Investigation: J.L.S., L.K., and P.P.J. Resources: L.K., L.L., and S.B.K. Visualization: J.L.S. and S.B.K. Writing—original draft: J.L.S. and S.B.K. Writing—review and editing: J.L.S., L.K., P.P.J., N.M., L.L., and S.B.K. Funding acquisition: S.B.K. Supervision: S.B.K. **Competing interests:** The authors declare that they have no competing interests. **Data and materials availability:** All data needed to evaluate the conclusions in the paper are present in the paper and/or the Supplementary Materials and can be found in Zenodo (http://doi.org/10.5281/zenodo.10994899).

Submitted 22 January 2024
Accepted 10 May 2024
Published 14 June 2024
10.1126/sciadv.ado2136